

# Producing slow light in warm alkali vapor using electromagnetically induced transparency

Kenneth DeRose<sup>†</sup>, Kefeng Jiang<sup>†</sup>, Jianqiao Li, Linzhao Zhuo, Scott Wenner, and Samir Bali\*

*Department of Physics, Miami University, Oxford, Ohio 45056-1866, USA*

We present undergraduate-friendly instructions on how to produce light pulses propagating through warm Rubidium vapor with speeds less than 400 m/s, i.e., nearly a million times slower than  $c$ . We elucidate the role played by electromagnetically induced transparency (EIT) in producing slow light pulses, and discuss how to achieve the required experimental conditions. The optical setup is presented, and details provided for preparation of pump, probe, and reference pulses of required size, frequency, intensity, temporal width, and polarization purity. Further details on suppressing residual magnetic fields below 0.2 mG over the entire laser-atom interaction region, are provided in the online Supplementary Materials.

© 2023 Optical Society of America

## 1. Introduction

It has been two decades since the first demonstration of slow optical pulses propagating through atomic media. [1, 2] Slow light was revealed as a striking consequence of a quantum mechanical phenomenon in light-matter interaction known as EIT, i.e., electromagnetically induced transparency. EIT arises from the interference between probability amplitudes for absorption pathways which are simultaneously excited by two resonant light fields - one strong, referred to as the pump (or coupling) field, and the other weak, referred to as the probe. [3, 4] EIT and slow light in warm alkali vapor continue to be central topics of research in quantum information and quantum technology, particularly for building robust quantum memories [5–7], and stable photon-shot-noise-limited electromagnetic field sensors using Rydberg atoms. [8] In Ref. [6], for instance, the authors provide an overview of current approaches to quantum memory, and state that “although all of these approaches have been studied and demonstrated, EIT remains the most popular scheme for quantum memory,” because, “in comparison to the other approaches, the EIT approach has a long storage time and is a relatively easy-to-implement and inexpensive solution”.

An excellent article on EIT-based experiments for undergraduate laboratories was published just over a decade ago. [9] Elegant EIT-based experiments carried out at undergraduate institutions have also been reported. [10] However, an undergraduate-friendly *experimental description of slow light* in atomic vapor does not exist. In this paper we endeavor to fill this gap. This is important because an increasing number of physics and engineering majors wish to get involved in the development of cutting-edge quantum technologies. There are several pedagogical advantages to introducing the concepts of EIT and slow light in an optics class for undergraduate seniors and first/second-year graduate students. For instance, in the advanced lecture/lab course “Optics and Laser Physics” that we teach at Miami University, students often ask, “We’ve read about laser applications in imaging, communications and medicine... can you tell us about *quantum* applications we haven’t heard of?” EIT and slow light can provide a satisfactorily impactful answer to this question. EIT physics is a natural extension to what these students have already been learning about light-matter

interaction. Early in the semester, they are introduced to population-rate equations for a laser system, which sets the stage for an EIT-based slow light system, since the simplest model for either system is provided by a three-level atom. Furthermore, students know about group versus phase velocity, and therefore have all the necessary background to learn about how a steep positive gradient of the refractive index within a narrow EIT spectral window can lead to a dramatically slow group velocity.

In this article, we state the relevant theoretical results for EIT and slow light, and describe our experimental setup for producing slow light pulses with group velocities less than 400 m/s. A price list for parts is included in the online Supplementary Material.

## 2. Theoretical description

The theory behind EIT and slow light has been explained in several high-quality undergraduate-friendly articles (see, for example, Refs. [9, 11–14]), including a textbook-treatment in Ref. [15] which is amenable to seniors. Here, we summarize the relevant results. A more complete derivation can be found in the online Supplementary Materials.

### A. Three-level atom model

Following the treatment in Ref. [15], we depict a fictitious three-level atom in Fig. 1, in which transitions are allowed between states 1 and 3 and between states 2 and 3, but not between states 1 and 2. This is the so-called lambda-system because the lower levels 1 and 2 have close-lying energies, resulting in a  $\Lambda$ -shaped configuration. The standard EIT experiment consists of a sample of such atoms illuminated by a strong coupling (or pump) laser of frequency  $\omega_c$  and a weak probe laser of frequency  $\omega_p$ , both tuned to near-resonance with  $|3\rangle$  from levels  $|2\rangle$  and  $|1\rangle$  respectively. The energy difference between levels 3 and 1 is  $\hbar\omega_{31}$ , and between 3 and 2 is  $\hbar\omega_{32}$ . The laser detunings are  $\Delta_c \equiv \omega_c - \omega_{32}$  and  $\Delta_p \equiv \omega_p - \omega_{31}$ . We assume that the pump beam only addresses the coupling transition  $|2\rangle \rightarrow |3\rangle$  and the probe beam only addresses the  $|1\rangle \rightarrow |3\rangle$  transition. The probe frequency is scanned around the (fixed) pump frequency, and the probe absorption is measured.

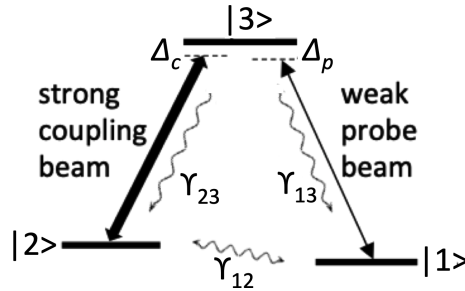


Fig. 1. Three-level atom in the  $\Lambda$ -shaped configuration. Excited state decay rates are denoted by  $\gamma_{13}$  and  $\gamma_{23}$ , and the ground state decoherence rate by  $\gamma_{12}$ .

In the Supplementary Materials, Sec. S1A - B, we write the Hamiltonian for an illuminated three-level atom, assuming that the incident field-induced electric dipole is the predominant light-atom interaction. We calculate the eigenenergies and eigenstates in Eq. (S9) - (S11), taking the pump and probe beams to be on-resonance for simplicity. One of the eigenstates is a “dark” state which is a coherent superposition of the two ground states  $|1\rangle$  and  $|2\rangle$ . This dark state has no quantum overlap with the excited state  $|3\rangle$ . Thus, an atom, once it is transferred to the dark state upon interaction with the light fields, stays there, no longer able to absorb a probe photon. Note that in the absence of the pump, the weak resonant probe would be

completely absorbed. Thus the pump laser “coherently prepares” the atoms to be transparent to the probe - this is EIT.

In order to calculate the spectral width of the transparency window, we must take into account the decay of the light-induced dipole moment due to various decohering processes (also called damping, or relaxation, processes). Such processes may arise from atomic motion which may, for example, cause the atom to leave the illuminated region, and the light-atom interaction to cease altogether. Similarly, elastic and inelastic collisions with other atoms and with the container walls, and other processes such as spontaneous emission, affect the phase and amplitude of the light-induced dipole moment. These mechanisms are discussed in more detail in Sec. 3B and C below. We denote all decay processes from  $3 \rightarrow 1$  and from  $3 \rightarrow 2$  by the optical decoherence rates  $\gamma_{13}$  and  $\gamma_{23}$ , respectively. The two ground states are close-lying, so that non-optical processes such as collisions may suffice to cause interchange between the two states - we denote this two-way  $1 \leftrightarrow 2$  decay by the ground state decoherence rate  $\gamma_{12}$ . In dilute samples where the densities are not so high that non-optical damping processes (e.g., collisions between ground state atoms) begin to dominate over optical damping processes e.g., spontaneous emission or Doppler broadening,  $\gamma_{12}$  is much smaller than  $\gamma_{13}$  and  $\gamma_{23}$ . This is an important requirement for EIT which is satisfied in our experiments, see Sec. 3C below.

We show in Sec. S1C - D of the Supplementary Materials that the density matrix formalism allows for simple phenomenological inclusion of decay processes into the calculation of the probe-induced atomic dipole moment and polarizability. This allows us to deduce the complex refractive index  $n(\omega_p) = n_r(\omega_p) + in_i(\omega_p)$ . The imaginary part  $n_i$  yields the absorption spectrum  $\alpha(\omega_p)$ . The complex refractive index is a convenient way to express something well-known: Where there is dispersion  $n_r(\omega)$ , there must be absorption  $\alpha$ . This is owing to causality-based Kramers-Kronig relations between the real and imaginary parts of the electric susceptibility  $\chi = \chi_r + i\chi_i$ . [16] We calculate the absorption  $\alpha(\omega_p)$  and real refractive index  $n_r(\omega_p)$  seen by the weak probe (see Eq. (S22) - (S23)) propagating through a sample of  $\Lambda$ -atoms which is coherently prepared by a strong pump beam in a dark state, as mentioned above. In the following sections we discuss some important limiting situations.

### B. Absorption and refractive index with pump field off

When the coupling field (or pump) is off, no EIT occurs. We obtain the usual results for probe absorption and real refractive index, which are plotted in Fig. 2 (a) and (b):

$$\alpha \xrightarrow{\Omega_c=0} \frac{N\omega_p}{\epsilon_0 c} \frac{|\mu_{13}|^2}{\hbar} \frac{\gamma_{13}}{\Delta_p^2 + \gamma_{13}^2} \quad (1)$$

$$n_r \xrightarrow{\Omega_c=0} 1 - \frac{N}{2\epsilon_0} \frac{|\mu_{13}|^2}{\hbar} \frac{\Delta_p}{\Delta_p^2 + \gamma_{13}^2} . \quad (2)$$

Here  $\Omega_c$  is the coupling beam Rabi frequency defined as  $\Omega_c \equiv \vec{d}_{32} \cdot \vec{\epsilon}_c E_c / 2\hbar$ , where  $\vec{d}_{32}$  is the transition dipole moment between levels  $|2\rangle$  and  $|3\rangle$ ,  $\vec{\epsilon}_c$  is the polarization of the coupling field, and  $\hbar$  is Planck's constant divided by  $2\pi$ . [17]  $N$  is the number of atomic dipoles per unit volume,  $c$  is the speed of light in vacuum,  $\epsilon_0$  is the electric permittivity of vacuum, and  $\mu_{13}$  is defined as the projection of the induced probe dipole moment on the direction of the probe field polarization.

Eq. (1), plotted in Fig. 2(a), depicts the expected Lorentzian absorptive line shape, with half width at half maximum (HWHM)  $\gamma_{13}$  and a maximum at  $\Delta_p = 0$ . Eq. (2), plotted in Fig. 2(b), depicts the expected dispersive line shape around probe-resonance, again with a HWHM of  $\gamma_{13}$ . In the immediate vicinity of resonance  $\Delta_p \approx 0$ , we see that  $n_r \rightarrow 1 - N|\mu_{13}|^2 \Delta_p / (2\epsilon_0 \hbar \gamma_{13}^2)$ , i.e.,  $n_r(\omega_p)$  has a negative slope. This is the well-known “anomalous dispersion” effect that occurs close to an atomic resonance and in which  $n_r$  decreases with increasing optical frequency. By contrast, as we move further away from resonance we see that

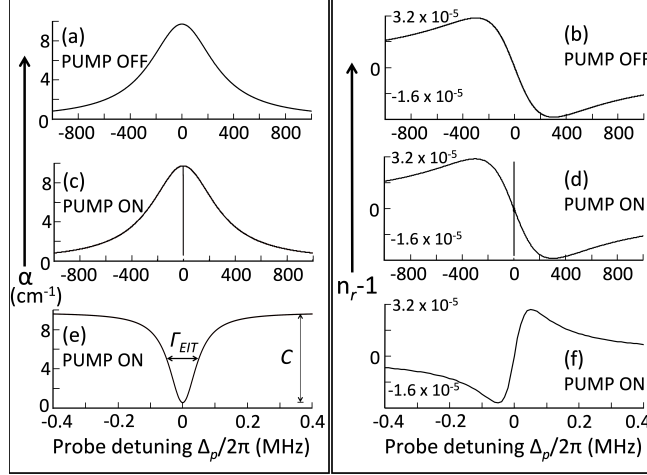


Fig. 2. The probe absorption coefficient  $\alpha$  (left panel) in  $\text{cm}^{-1}$  and real refractive index  $n_r$  (right panel), versus probe detuning  $\Delta_p = \omega_p - \omega_{31}$  as predicted by Eq. (1-4). (a, b) The case of “no pump” from Eq. (1) and Eq. (2). (c, d) The “EIT case” from Eq. (3) and Eq. (4) with parameter-values from our experiments:  $\Delta_c = 0$ ,  $|\Omega_c|/2\pi = 4$  MHz,  $\omega_p/2\pi = 3.77 \times 10^{14}$  Hz,  $N = 3.36 \times 10^{11}/\text{cm}^3$ ,  $\gamma_{13}/2\pi = 300$  MHz,  $\gamma_{12}/2\pi = 3$  kHz,  $|\mu_{13}| = 2.54 \times 10^{-29}$  C.m. (e, f) Magnified view of sharp EIT features in c and d.

$n_r$  increases with frequency on either side. This is normal dispersion, consistent with the classic experiment of propagating white light through a glass prism and observing that red light deviates the least and blue the most.

### C. Absorption and refractive index with pump field on

When the strong coupling field is on, and assumed to be on-resonance for simplicity ( $\Delta_c = 0$ ), we obtain for the probe absorption  $\alpha(\omega_p)$  and real refractive index  $n_r(\omega_p)$  in the “weak-probe approximation” ( $\Omega_p \ll \Omega_c$ ; here  $\Omega_p$  is the probe Rabi frequency and is defined as  $\Omega_p \equiv \vec{d}_{31} \cdot \vec{\epsilon}_p E_p / 2\hbar$ , where  $\vec{d}_{31}$  is the transition dipole moment between levels  $|1\rangle$  and  $|3\rangle$ , and  $\vec{\epsilon}_p$  is the polarization of the probe field): [17]

$$\alpha(\omega_p) = \frac{N\omega_p |\mu_{13}|^2}{\epsilon_0 c \hbar} \times \frac{\gamma_{13}\Delta_p^2 + \gamma_{12}(\gamma_{12}\gamma_{13} + |\Omega_c|^2)}{[\Delta_p^2 - \gamma_{12}\gamma_{13} - |\Omega_c|^2]^2 + \Delta_p^2[\gamma_{12} + \gamma_{13}]^2} \quad (3)$$

$$n_r(\omega_p) = 1 - \frac{N}{2\epsilon_0} \frac{|\mu_{13}|^2}{\hbar} \times \frac{\Delta_p(\Delta_p^2 - |\Omega_c|^2 + \gamma_{12}^2)}{[\Delta_p^2 - \gamma_{12}\gamma_{13} - |\Omega_c|^2]^2 + \Delta_p^2[\gamma_{12} + \gamma_{13}]^2}. \quad (4)$$

Eq. (3-4) are plotted in Figs. 2(c) - (f). Eq. (S22) and Eq. (S23) are generalized forms of Eq. (3) and Eq. (4) for  $\Delta_c \neq 0$ .

The absorption  $\alpha$  and refractive index  $n_r$  in the lower panels of Fig. 2 are strikingly different from the top panel where the coupling field is off. It is instructive to verify that Eq. (1-4) satisfy the Kramers-Kronig relations between  $\chi_r = 2(n_r - 1)$  and  $\chi_i = c\alpha/\omega_p$ , namely,  $\chi_r(\omega_p) = (2/\pi) \int_0^\infty d\omega \frac{\omega \chi_i(\omega)}{\omega^2 - \omega_p^2}$  and  $\chi_i(\omega_p) = (2/\pi) \int_0^\infty d\omega \frac{\omega_p \chi_r(\omega)}{\omega_p^2 - \omega^2}$ .

#### D. The EIT “window”

EIT manifests itself as a dramatic drop in absorption  $\alpha(\omega_p)$  in Figs. 2 (c, e) when the coupling and probe beams are on-resonance. In our experiments,  $\gamma_{12}/2\pi \sim \text{few kHz}$ ,  $|\Omega_c|/2\pi \sim \text{few MHz}$ ,  $\gamma_{13}/2\pi \sim \text{few hundred MHz}$ , and  $|\Delta_p|/2\pi \leq 100 \text{ kHz}$ , so that we verify the “strong coupling field approximation”:

$$|\Omega_c| \gg |\Delta_p|, \gamma_{12} \quad (5)$$

which is one of two conditions (see Eq. (11) below) that  $\Omega_c$  must satisfy in order to produce slow light. Using  $\gamma_{12} \ll \gamma_{13}$ , we find from Eq. (3), in the  $\Delta_p \rightarrow 0$  limit :

$$\alpha \rightarrow \frac{N\omega_p}{\epsilon_0 c} \frac{|\mu_{13}|^2}{\hbar} \frac{\gamma_{12}}{|\Omega_c|^2} \approx 0 \quad (6)$$

which yields transparency in a narrow “EIT window”.

In order to simply obtain an approximate expression for the EIT linewidth  $\Gamma_{EIT}$  (see Fig. 2e) it is convenient to set  $\Delta_p = 0$  in Eq. (S22) while allowing  $\Delta_c$  to vary around the resonance condition  $\Delta_p - \Delta_c = 0$  (also known as the Raman, or two-photon, resonance condition):

$$\alpha \xrightarrow{\Delta_p=0} \alpha_{\Omega_c=0} \left[ 1 - \frac{|\Omega_c|^2}{\gamma_{13}} \frac{\gamma_{12} + \frac{|\Omega_c|^2}{\gamma_{13}}}{\Delta_c^2 + \left( \gamma_{12} + \frac{|\Omega_c|^2}{\gamma_{13}} \right)^2} \right], \quad (7)$$

where  $\alpha_{\Omega_c=0} = N\omega_p|\mu_{13}|^2/(\epsilon_0 c \hbar \gamma_{13})$  is obtained by setting  $\Delta_p = 0$  in Eq. (1). The first term inside the parentheses in Eq. (7) represents the baseline absorption without EIT. The second term is the EIT window depicted in Fig. 2(e), which is a Lorentzian with full-width-half-maximum  $\Gamma_{EIT}$  given by:

$$\Gamma_{EIT} = 2 \left( \gamma_{12} + \frac{|\Omega_c|^2}{\gamma_{13}} \right). \quad (8)$$

In Eq. (8),  $\Omega_c$  depends on the pump intensity  $I$  (see Eq. (16) below), so that the EIT window broadens when the intensity of the pump beam increases. Upon substituting typical experimental parameter-values (see caption under Fig. 2) into the approximate expression in Eq. (8), we predict  $\Gamma_{EIT} \approx 100 \text{ kHz}$  for the EIT window. This is in close agreement with Eq. (3) which is plotted in Fig. 2(e), as revealed by direct inspection of the figure. The probe absorption  $\alpha$  is minimum when  $\Delta_c$  is minimum, so that an expression for the EIT contrast, or amplitude of the transparency window, denoted by  $C$  (see Fig. 2e) may be simply obtained by setting  $\Delta_c = 0$  in the second term of Eq. (7):  $C = |\Omega_c|^2/(\gamma_{13}\gamma_{12} + |\Omega_c|^2)$  which, in the strong coupling approximation (Eq. (5)), predicts  $\approx 100\%$  transparency.

In practice, the observed contrast and linewidth are much lower (see Sec. 6). This is because, in steady-state the fraction of atoms settling in the dark state is significantly reduced for reasons discussed in Sec. 3B. In short, our theory is based on a closed three-level model, whereas, in real atoms, many energy levels are addressed by the laser fields. This provides extraneous energy-levels to which the population can leak, severely reducing contrast (in our experiments the maximum contrast is about 25%). The lowered contrast, in turn, leads to a significant reduction in the observed EIT linewidth: Only the probe spectral components which lie at the center of the EIT window can propagate through and are detectable in transmission even though considerably reduced in intensity, while frequency components near the edge of the window are too heavily attenuated to be detected. [18, 19] In Ref. [18] it is shown that the power-broadened component of the linewidth in Eq. (8) is estimated to reduce by a factor  $\sqrt{OD}$ , where  $OD$  is the on-resonance optical depth seen by the probe as it traverses an atom sample of length  $L$  (with the coupling beam turned off; see Supplementary Notes, Sec. S1 D). The  $OD$  is defined by the product of  $L$  with the on-resonance probe

absorption  $\alpha_{\Omega_c=0}$  (see Eq. (7) above):  $OD = L\alpha_{\Omega_c=0} = N\omega_p|\mu_{13}|^2L/(\epsilon_0c\hbar\gamma_{13})$ . To take this attenuation into account, we amend Eq. (8) to

$$\Gamma_{EIT} = 2 \left( \gamma_{12} + \frac{|\Omega_c|^2}{\gamma_{13}\sqrt{OD}} \right), \quad (9)$$

where the power-broadened term is identical to Eq. (5) in Ref. [5] and Eq. (2) in Ref. [18].

#### E. The refractive index and slow light

We shift focus now to the real refractive index  $n_r$  (Eq. (4)), plotted in Fig. 2 (d, f). In particular, using Eq. (5), we find that a strong coupling field induces a *positive* slope in  $n_r$  within the narrow EIT window,

$$n_r \rightarrow 1 + \frac{N}{2\epsilon_0} \frac{|\mu_{13}|^2}{\hbar} \frac{\Delta_p}{|\Omega_c|^2}, \quad (10)$$

as clearly depicted in Fig. 2 (f). We see from Eq. (10) that, if we ensure that the coupling field satisfies the condition

$$|\Omega_c|^2 << \frac{N|\mu_{13}|^2}{2\epsilon_0\hbar} \omega_p, \quad (11)$$

we may produce a steep positive gradient about  $\Delta_p \sim 0$ .

The group velocity of light  $v_g$  is defined by the relation  $v_g/c \equiv (n_r + \omega_p dn_r/d\omega_p)^{-1}$ . A steep positive gradient therefore leads to a significantly reduced group velocity for the probe. Applying Eq. (10 - 11), we have

$$\frac{v_g}{c} \approx |\Omega_c|^2 / \left( \frac{N|\mu_{13}|^2}{2\epsilon_0\hbar} \omega_p \right) << 1. \quad (12)$$

From the definition of the on-resonance optical depth  $OD$  above, and assuming that the power-broadened term in Eq. (9) is dominant, we may re-cast Eq. (12) as

$$\frac{v_g}{c} = \frac{\Gamma_{EIT}}{\sqrt{OD}} \frac{L}{c} \propto \frac{I}{N}, \quad (13)$$

where we have used Eq. 16. This means that the probe light is delayed by a time  $\tau_d$ , given by: [19]

$$\tau_d = \frac{L}{v_g} \sim \frac{\sqrt{OD}}{\Gamma_{EIT}} \propto \frac{NL}{I}. \quad (14)$$

Thus, the narrower the EIT window the larger the pulse-delay  $\tau_d$ . [20] See Ref. [21] and Sec. 4.1 of Ref. [5] for more accurate predictions of the maximum achievable  $\tau_d$ , that are achieved by making detailed measurements of the EIT lineshape and contrast, and incorporating some of these empirical values into the theory.

We wish to clarify a couple issues that often confuse students. First, the dramatic changes in  $n_r$  near resonance do not much impact the *phase velocity* of light ( $c/n_r$ ), because  $n_r$  never significantly departs from unity for a dilute vapor - this is clearly visible in Fig. 2 (d, f). No physical significance is ascribed to the phase velocity, so that the fact that  $n_r$  dips below unity, causing the phase velocity to exceed  $c$ , is no cause for alarm. Second, the definition of  $v_g$  above suggests that when  $dn_r/d\omega$  is negative, as is the case near-resonance just outside the EIT window, the group velocity may, in principle, exceed the phase velocity and even  $c$ . However, just outside the EIT window also happens to be where the absorption is high, thus no signal is actually able to propagate faster than  $c$ . [14] In the context of our experiments, recall the discussion in the previous sub-section of EIT linewidth narrowing owing to low EIT contrast, where we pointed out that even probe spectral components that lie within the EIT window but not near the center are too heavily attenuated to be detectable in transmission, let alone components outside the transparency window.

### F. Stored light and EIT-based quantum memory

In effect, a pulse of probe light is slowed and stored in the sample for a time  $\tau_d$  [19], and the medium then acts as a quantum memory where information can be stored. A variety of schemes, some not based on EIT, have reported values of  $\tau_d$  ranging from  $\mu\text{s}$  to  $\text{ms}$ , and even higher [6]. Notice that the pulse undergoes a dramatic spatial compression inside the sample: The front end slows down upon entry into the sample and propagates at  $v_g$ , even as the pulse-rear, which is still outside, propagates at  $c$ . The compression factor is given by  $L_p/L_0 = v_g/c$  where  $L_p$  is the length of the compressed pulse inside the medium and  $L_0$  is the free-space pulse length. [19]

However, from Sec. 2D it is clear that Eq. (14) and the subsequent discussion apply only to a probe pulse for which the frequency bandwidth  $\tau_p^{-1}$  fits within the EIT linewidth  $\Gamma_{\text{EIT}}$ , i.e. for a pulse such that  $\tau_p^{-1} \leq \Gamma_{\text{EIT}}$ . In other words, if  $\tau_p$  is so short that the probe bandwidth is broader than  $\Gamma_{\text{EIT}}$ , then the probe frequency components outside the transparency window suffer significant absorption, causing the pulse to become distorted. Substituting this condition in Eq. (14) we find: [22]

$$\tau_p^{-1} \tau_d \leq \sqrt{OD}. \quad (15)$$

This relation between the bandwidth of the probe pulse and the pulse delay is known as the “delay-bandwidth product”, which is a figure of merit for a storage/memory device, as it is a measure of how many probe pulses fit within the sample (without being absorbed to the extent that they undergo distortion). [5,19] A drawback of EIT-based quantum memory is that, owing to the narrow bandwidth requirements of EIT, this product remains low, e.g., for our longest observed  $\tau_d$  of  $68 \mu\text{s}$  (see Fig. 9b) and  $\tau_p = 170 \mu\text{s}$  (see Sec. 4E), the delay-bandwidth product is 0.4. In our experiments,  $\sqrt{OD} \approx 5$  (see Sec. 7A), so Eq. (15) is satisfied. Our  $OD$  and delay-bandwidth product are comparable to previous values reported for EIT-based quantum memory in warm  $^{87}\text{Rb}$  vapor. [5,23] On the other hand, non EIT-based techniques in the same medium have yielded a delay-bandwidth product that is two orders of magnitude higher. [5,24]

### 3. Three-level atoms: Implementation in the lab

In the lab, Rubidium is a popular choice of alkali, owing to the ready availability of inexpensive single mode diode lasers at the resonance wavelength for transitions from the  $5^2S_{1/2}$  ground state to the  $5^2P_{1/2}$  excited state (D1-transition; 795 nm) or the  $5^2P_{3/2}$  excited state (D2-transition; 780 nm). Fig. 3 shows the hyperfine energy-level structure for both stable isotopes  $^{85}\text{Rb}$  (nuclear spin  $I = 5/2$ ) and  $^{87}\text{Rb}$  ( $I = 7/2$ ). [25]

Our experiments are performed on the D1 transition  $5^2S_{1/2}, F_g = 2 \rightarrow 5^2P_{1/2}, F_e = 1$  in  $^{87}\text{Rb}$  atoms. The hyperfine D1 transition for  $^{87}\text{Rb}$  involves the  $5^2S_{1/2}$  ground state and the  $5^2P_{1/2}$  excited state, which are split by the interaction of the valence electron’s total angular momentum (orbital + spin) with the nuclear spin, creating  $F_g = 1, 2$  ground energy states (separated by 6.8 GHz), and  $F_e = 1, 2$  excited energy states (separated by 815 MHz). Each hyperfine state  $F$  has  $2F + 1$  degenerate substates with quantum number  $m_F$  ranging from  $m_F = -F$  to  $F$  in increments of 1. Measurement will find the atom with an angular momentum component  $m\hbar$  along a chosen quantization axis - we choose  $z$  as our axis of quantization. For the  $F_g = 2$  ground state, for example, five magnetic substates are revealed in the presence of a weak external magnetic field  $B_z$  (along  $z$ ) which lifts the degeneracy by imparting a Zeeman shift  $\Delta E = g_f \mu_B m_{F_g} B_z$  to each magnetic sub-level. Here  $g_f$  is the Lande g-factor for the hyperfine state ( $g_f = 1/2$  for  $F_g = 2$ ),  $\mu_B$  is the Bohr magneton ( $9.274 \times 10^{-28}$  Joules/Gauss), and  $m_{F_g}$  is the magnetic sub-level number. The Zeeman shifts between the magnetic sub-levels of the  $F_g = 2$  ground state are 0.7 kHz/mG. [25]

A pump or probe laser tuned near-resonance to a particular  $F_g \rightarrow F_e$  transition pumps other close-lying  $F_e$  states off-resonantly, creating extraneous channels for atomic population leakage, which diminishes the steady-state fraction of atoms in the dark state. The  $^{87}\text{Rb}$  D1 transition is advantageous in that respect

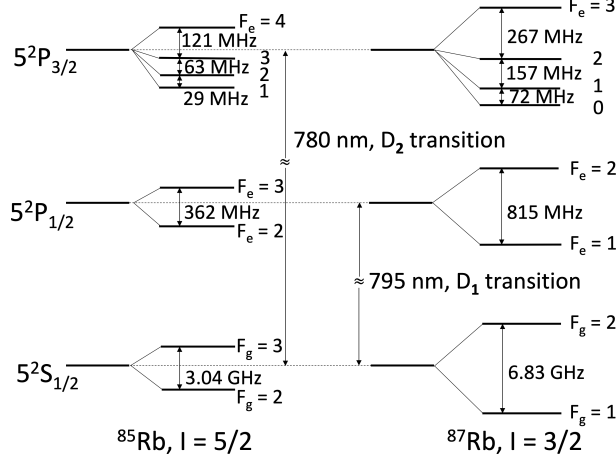


Fig. 3. Rb energy-levels with hyperfine structure.

because the  $F_e$  level-separation of 815 MHz is largest, compared to that of the D1 transition in  $^{85}\text{Rb}$  (362 MHz), and of the D2 transitions (Fig. 3). See Sec. 4C for further details.

#### A. Zeeman EIT: Spin polarization via optical pumping

Three-level schemes with alkali atoms for EIT-based slow light experiments fall into two categories: Hyperfine EIT and Zeeman EIT. Hyperfine EIT with  $^{87}\text{Rb}$  is depicted in Fig. 4 (a). A strong pump beam (coupling laser; solid line) is tuned to one  $F_g \rightarrow F_e$  transition, while a weak beam (probe; dashed line) is tuned to the other transition, 6.83 GHz apart. The probe is created by splitting off a small amount from the coupling beam, using an expensive electro-optic modulator. Alternatively, one may employ two phase-locked lasers, each tuned to either transition. Zeeman EIT, depicted in Fig. 4 (b), is less resource-intensive, requiring a single passively-stable laser system and less expensive acousto-optical modulators. Hence, we confine our attention to this method. Zeeman EIT relies upon the optical pumping of the magnetic Zeeman sub-levels created by applying  $B_z$ , using a strong coupling beam and a weak probe beam of mutually orthogonal circular-polarization (one beam  $\sigma^+$ , the other  $\sigma^-$ ). Both beams propagate collinearly with  $B_z$ .

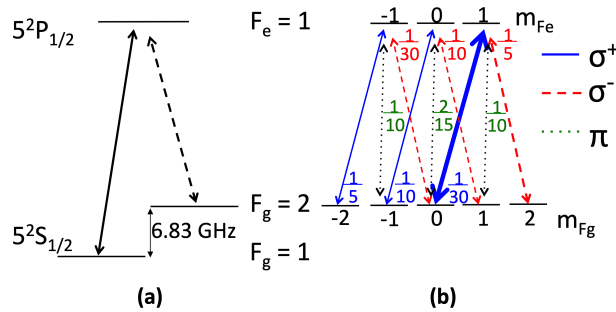


Fig. 4. Three-level lambda schemes for a) hyperfine EIT and b) Zeeman EIT. In (b) the transition strength between a pair of magnetic sub-states depends on both the light polarization and the magnetic quantum numbers of the two levels involved. The relative strengths are indicated for  $\sigma^+$  (solid lines),  $\sigma^-$  (dashed lines), and linear ( $\pi$ ; dotted lines) polarizations of light. [25, 26] The ground states  $m_{F_g} = 2, 0$  and the excited state  $m_{F_e} = 1$  approximate the three levels  $|1\rangle, |2\rangle, |3\rangle$  in Fig. 1(a), respectively.

Fig. 4(b) depicts a strong  $\sigma^+$  coupling field (solid arrows) and weak  $\sigma^-$  probe field (dashed arrows),



tuned to near-resonance with the  $5^2S_{1/2}, F_g = 2 \rightarrow 5^2P_{1/2}, F_e = 1$  transition. [25, 26] The dipole selection rules for transitions induced between magnetic substates by  $\sigma^+$  ( $\sigma^-$ ) light are  $\Delta m = +1$  ( $-1$ ) for absorption and  $\Delta m = -1$  ( $+1$ ) for stimulated emission, in addition to the  $\Delta m = 0, \pm 1$  selection rule for spontaneous emission transitions. [25] This means that after many absorption-emission cycles have occurred, the strong  $\sigma^+$  field optically pumps the atoms into the  $m_{F_g} = 0$  sub-state. From here, the pump excites the atoms to the  $m_{F_e} = 1$  sub-state, which is followed either by spontaneous decay to the  $m_{F_g} = 1, 2$  spin sub-states (where they stay) or by emission back into the  $m_{F_g} = 0$  state (in which case they are re-excited). Eventually, after a time that is long compared to the excited state lifetime of 27.7 ns for the Rb D1 line, the atoms accumulate into the  $m_{F_g} = 1, 2$  spin sub-states (typically, after pumping on a time-scale of ms). The action of the weak  $\sigma^-$  probe is to optically pump some of these atoms toward lower  $m_{F_g}$ -states. Eventually, in the steady-state, the atomic population is concentrated in the  $m_{F_g} = 0, 2$  spin sub-states. Thus the atom is “spin-polarized” via optical pumping. [27]

Indeed, the ideal three-level lambda system (states  $|1\rangle$ ,  $|2\rangle$ , and  $|3\rangle$  in Fig. 1) is well-approximated by the ground states  $m_{F_g} = 2, 0$  and the excited state  $m_{F_e} = 1$ . In Fig. 4(b) the pump (thick solid arrow) and probe (rightmost dashed arrow) are highlighted. The method for fine-tuning the pump and probe laser frequencies to resonance with these particular Zeeman sub-levels is described in Sec. 4C. These approximate three-level atoms then evolve into the dark state, enabling EIT and slow light. Factors causing spin relaxation that reduce the dark state population are discussed in Sec. 3B below.

Note that the assumption made at the beginning of Sec. 2, that the coupling beam only addresses levels  $|2\rangle$  and  $|3\rangle$ , and the probe beam only addresses levels  $|1\rangle$  and  $|3\rangle$ , is automatically satisfied in Zeeman EIT because  $\sigma^+$  pump photons cannot be absorbed by the  $|m_{F_g} = 2\rangle \rightarrow |m_{F_e} = 1\rangle$  transition and  $\sigma^-$  probe photons cannot be absorbed by the  $|m_{F_g} = 0\rangle \rightarrow |m_{F_e} = 1\rangle$  transition.

### B. Spin relaxation mechanisms: Role of buffer gas

There are several spin depolarization mechanisms that reduce the EIT contrast and affect its linewidth. The spin-polarized Rb atoms prepared in the previous subsection exist within the sample volume that is jointly illuminated by the pump and probe beams. In a glass cell filled with warm alkali vapor, just the central part of the cell is typically illuminated. The atoms are moving at thermal speeds, causing the polarized atoms to transit through the laser beams and exit the illuminated volume. A collision with the glass wall destroys their polarization [28], and the unpolarized atoms may subsequently re-enter the illuminated region. These transit-time effects reduce the sample polarization. [29] Further, there are spin-exchange collisions between spin-polarized Rb atoms which can redistribute the populations in the magnetic sub-states, causing depolarization. [28]

There are two commonly used approaches [27] to suppress the spin-depolarizing effects described above: i) include an inert buffer gas such as Ne, He, or Ar in the Rb vapor cell, or ii) coat the inside of the glass vapor cell with an anti-relaxation coating such as paraffin.

Coated cells can yield significantly longer spin coherence times than buffer gas cells because the paraffin coating suppresses the Rb spin-depolarization via “softer” atom-wall collisions. However, the light-Rb atom interaction dynamics in coated cells is more complicated, yielding a dual-structured EIT lineshape with a narrow central peak sitting atop a broad pedestal (see for example Ref. [5] and references cited therein). The broad pedestal is due to Rb atoms interacting with light during a one-time pass through the light beams. The narrow peak, on the other hand, results from contributions by polarized Rb atoms that transit in and out repeatedly through the laser beams, interacting coherently each time with the pump and probe fields. These atoms make many wall collisions before eventually becoming depolarized. The linewidth of the narrow peak is significantly affected by factors such as the coating quality and cell geometry. [5] In the work reported

here we do not use coated cells.

In buffer gas cells, the usual practice for EIT and slow light experiments is to mix noble gas (up to several tens of Torr) with a few microTorr of Rb. [5] In our experiments we use 10 Torr of Ne. Frequent Rb-Ne collisions reduce the Rb atoms' mean free path to values much smaller than the pump beam diameter [30], thus confining the atoms within the illuminated volume. Instead of flying through the laser beam at thermal speeds in the absence of a buffer gas, the atoms then slowly diffuse through, thereby increasing the laser-atom interaction time by several orders of magnitude. [5] Note that Rb-Ne collisions cause the spin-polarized Rb atom's velocity to change, but with negligible spin relaxation. Such collisions that rapidly redistribute the atomic velocities without re-equilibrating the populations of the atomic levels are termed "velocity-changing collisions" in the literature. [27,30] Rb-Rb and Rb-wall collisions are negligible compared to Rb-Ne collisions.

Still, decoherence effects remain that are not addressed by the buffer gas (or by wall coatings). Inhomogeneities in the magnetic field used for Zeeman EIT cause spatial variation of the dark state leading to absorption. In Sec. S2 of the Supplementary Materials we discuss how to suppress these inhomogeneities. Furthermore, an incoherent pumping mechanism, known as radiation trapping, may become significant at high atomic densities. Radiation trapping refers to the reabsorption of spontaneously emitted photons within the illuminated volume, and is expected to become significant inside our probe beam radius at number densities  $N \geq 5 \times 10^{11}/\text{cm}^3$  (see Sec. 4 D). [31] Hence, we keep our number density below this value (see Sec. 5 and Sec. S2 D).

### C. Slow light conditions; estimate of $\gamma_{12}$ , $\gamma_{13}$

Let us examine how the conditions for slow light, Eq. (5) and Eq. (11), are satisfied in our experiments. The relation between the Rabi frequency  $\Omega_c$  and coupling beam intensity  $I$ , in the case of the spin-polarized atom in Fig. 4(b), is defined through the well-known expression for the saturation intensity  $I_{sat}$ : [17,25,32]

$$\frac{(2|\Omega_c|)^2}{\Gamma^2} \equiv \frac{I}{2I_{sat}}, \quad \text{where } I_{sat} = \frac{\pi\hbar c}{3\lambda^3} \Gamma. \quad (16)$$

Here  $\lambda$  is the optical wavelength for the transition, and  $\Gamma$  is the natural linewidth due to spontaneous emission. [25]  $I_{sat}$  is the excitation intensity at which the stimulated emission rate is half the spontaneous emission rate. For the  $^{87}\text{Rb}$  D1 transition,  $\Gamma = 2\pi$  (5.75 MHz) and  $\lambda = 794.98$  nm ( $\omega_p/2\pi = 3.77 \times 10^{14}$  Hz), yielding  $I_{sat} = 1.5$  mW/cm<sup>2</sup>. [25] Our pump intensity  $I$  mostly varies between 1.25 and 5.6 mW/cm<sup>2</sup> (see Sec. 4 D), which means  $|\Omega_c|/2\pi$  ranges from 1.9 MHz to 3.9 MHz.

The ground state decoherence rate  $\gamma_{12}$  arises from Rb-Rb collisions, Rb collisions with the cell walls, and from Rb atoms eventually diffusing out of the illuminated volume despite the buffer gas. Collisions with the inert buffer gas do not contribute significantly to  $\gamma_{12}$ . However, since our experiments use Zeeman hyperfine levels, inhomogeneities in the magnetic field contribute to  $\gamma_{12}$ . Good suppression of stray magnetic fields (Sec. S2, Supplementary Materials), results in a value  $\gamma_{12} \approx 3$  kHz, as reported in the literature. [33,34] Clearly,  $\Omega_c \gg \gamma_{12}$ , and since  $\Delta_p/2\pi \sim 100$  kHz or less (see Figs. 2 (e,f) and 8) our experiments fall in the strong coupling intensity regime, i.e., the condition in Eq. (5) is well-satisfied.

Next, to check that Eq. (11) is also well-satisfied in our experiments, we note that the dipole matrix element  $|\mu_{13}|$  for the  $^{87}\text{Rb}$  D1 transition in our spin-polarized atom is well-approximated by just the magnetic quantum number-independent value (known as the reduced matrix element)  $2.54 \times 10^{-29}$  Cm. [25] The number density  $N$  is  $\sim 1.5 - 3.4 \times 10^{11}/\text{cm}^3$  (see Sec. 5), yielding  $(1/2\pi)\sqrt{N}|\mu_{13}|^2\omega_p/(2\epsilon_0\hbar) \approx 2 - 4$  GHz, which exceeds the  $|\Omega_c|/2\pi$ -values above by three orders of magnitude.

Finally, we estimate the excited state damping  $\gamma_{13}$  which arises from the spontaneous emission rate  $\Gamma$ , the dephasing  $\gamma_{coll}$  due to Rb collisions with the buffer gas, and the Doppler broadening  $\Gamma_D$ . Recall from Eq. 1 and Fig. 2 (a) that  $2\gamma_{13}$  is manifested as the width of the absorption peak. Our sample consists of

a few  $\mu\text{Torr}$  of isotopically enriched dilute  $^{87}\text{Rb}$  vapor mixed with 10 Torr of Ne buffer gas. To estimate  $\gamma_{\text{coll}}$  we follow the empirical relation  $2\gamma_{\text{coll}}/2\pi = 9.84 \text{ MHz/Torr}$  derived in Ref. [35]. We see that, for 10 Torr of Ne,  $\gamma_{\text{coll}}/2\pi \sim 50 \text{ MHz}$ . On the other hand, the Doppler broadening of the absorption profile of Rb vapor, illuminated by a frequency-scanning monochromatic beam, arises due to the thermal motion of the atoms. [36] In a simple 1D situation, an atom moving with thermal velocity  $v_{th}$  toward or away from a laser beam of frequency  $\omega_0$  sees a Doppler-shifted frequency  $\omega_0(1 \pm v_{th}/c)$ . This means that for a thermal distribution of velocities we may estimate the full width at half maximum (FWHM),  $\Gamma_D$ , of the Doppler broadened absorption profile to be  $\Gamma_D = 2\omega_0 v_{th}/c = 2k v_{th}$ . Here  $k = 2\pi/\lambda$  is the magnitude of the incident field wave vector. If we use the most probable velocity  $v_{th} = \sqrt{(2\ln 2) k_B T/m}$ , we obtain  $v_{th} \approx 200 \text{ m/s}$  at  $T = 293 \text{ K}$ , yielding  $\Gamma_D/2 \approx 2\pi(250 \text{ MHz})$  at  $\lambda = 795 \text{ nm}$ . Thus  $\gamma_{13}$  is dominated by  $\gamma_{\text{coll}}$  and  $\Gamma_D/2$  (both are significantly larger than  $\Gamma$ ). We use their sum as an estimate for  $\gamma_{13}$ .

Note from Eq. (9) and Eq. (13), that, in the high coupling intensity limit, both  $v_g$  and  $\Gamma_{\text{EIT}}$  decrease linearly with the intensity. However, lowering the intensity too far (although still in the high intensity limit) may reduce the steady-state population in the dark state enough that slow light effects start to degrade, causing the probe pulse to distort and appear to speed up again. Thus we may expect a sweet spot in the pump intensity, where conditions for slow light are optimized (see Sec. 7 C).

#### 4. Experimental setup

We describe how we create pump, probe, and reference beams, tuned to the appropriate alkali transitions for Zeeman EIT shown in Fig. 4(b), and of the required size, intensity, frequency, temporal width, and polarization purity. Our optical layout is depicted in Fig. 5.

##### A. Laser source

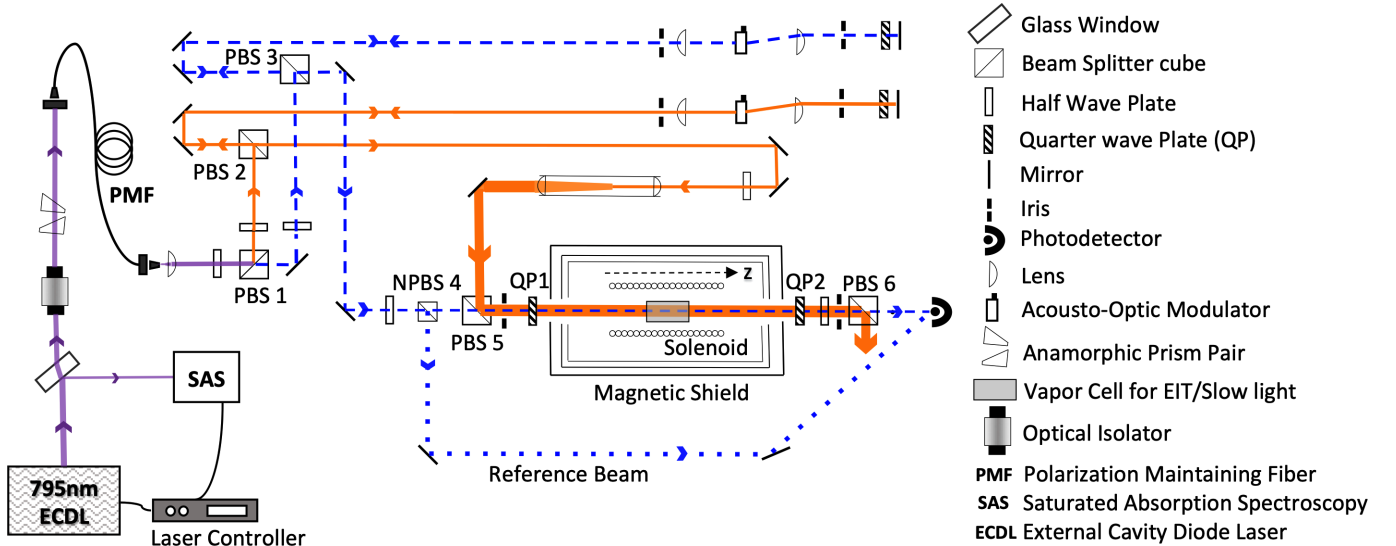


Fig. 5. Optical setup. The laser is split at a polarizing beamsplitter (PBS 1) into a strong pump, or coupling, beam (solid lines) and a weak probe beam (dashed lines). Before entering the vapor cell the probe beam is split at a non-polarizing beamsplitter (NPBS 4) to create a reference beam (dotted lines) for the slow light measurement. The  $z$ -axis is indicated.

We use a commercial external cavity tunable diode laser (ECDL) to provide linearly polarized continuous-wave light at  $\sim 795 \text{ nm}$ . A few percent of the output is split off for use in a saturated absorption spectroscopy

(SAS) set-up to enable the precise tuning of the laser to the  $F_g = 2 \rightarrow F_e = 1$  D1 transition, as described below.

The main ECDL output is first passed through a Faraday rotation-based optical isolator (OI) which optically isolates the laser from back reflections (e.g., arising from the optics that couple the light into the fiber). The light then passes through an anamorphic prism pair to circularize the elliptical cross-section of the beam, before coupling into a single-mode polarization-maintaining fiber which preserves the direction of the linear polarization of the input beam (we measured a residual drift of  $< 2\%$  in the polarization direction at the fiber output). The single-mode fiber is typically aligned and operated in most labs at a transmission efficiency of only 30 – 50%, but produces a clean Gaussian spatial profile. Gaussian spatial profiles are highly desirable for pump-probe experiments where the pump and probe beams must be well-collimated, and must have good spatial overlap that is amenable to quantitative modeling.

### *B. Creating the pump and frequency-scannable probe*

The output from the fiber ( $\sim 7$  mW) is collimated using an aspheric lens. The collimated light is divided by a polarizing beamsplitter (PBS 1) into two orthogonally linearly polarized beams - the strong coupling (or pump) beam (solid line) and weak probe beam (dashed line).

In pump-probe spectroscopy the probe is swept in frequency around the fixed pump frequency, and the probe transmission spectrum is detected. The sweeping is accomplished with an acousto-optic modulator (AOM), which is a device that uses a sound wave propagating through a crystal to form a diffraction grating for incoming light waves, producing frequency-upshifted (+1) and downshifted (−1) orders, in addition to the 0 order at the incident frequency. [16,37] The  $\pm 1$  orders emanate at a slight angle to the direction of the incident beam, symmetrically on either side, while the 0 order continues along the incident beam direction. By carefully aligning the angle of incidence of the beam on the AOM, we achieve about 70% of the incident power in the first order of choice, with most of the remaining power in the 0 order, while a small amount leaks into the undesired first order. The AOM performs a frequency-scan by introducing a fixed offset (80 MHz in our case) and sweeping back and forth about that fixed offset value by some desired amount (chosen by user, anywhere from zero up to a maximum sweep  $\pm 20$  MHz for our model). For the purpose of measuring the EIT linewidth in Fig. 2 (c) and (e), a sweep of  $\pm 100$  kHz suffices (see Fig. 8). Because of the fixed frequency-offset of 80 MHz that the AOM introduces, we must insert an identically configured AOM in the path of the pump beam as well, so that both the pump and probe beams are offset in frequency by the same amount. To drive the AOMs a dual-output waveform generator which creates twin phase-locked identical 80 MHz, 1 V signals is used. Before feeding to the AOM, each signal is amplified using a standard RF amplifier. Planoconvex lenses of focal length 30 cm are placed on either side of each AOM, with the AOM crystal located at the common focal spot.

One problem encountered is that the angle of the diffracted orders changes when the output frequency is varied, causing a spatial shift in the beam at the vapor cell located a few feet downstream. This shift is a problem because the probe beam moves off the center of the vapor cell during the course of its frequency scan. To overcome this problem, the desired diffracted order is retroreflected back through the crystal (see top right hand corner of Fig. 5), such that the double-shifted order is aligned with the incident beam but in the counter-propagating direction. [37] For this double-shifted beam the angular deflection from the second pass cancels the deflection from the first pass. The cancellation is not ideal, due to unavoidable imperfections in alignment, but the spatial shifting of the scanning probe at the site of the vapor cell is highly suppressed in this double-pass AOM configuration. The presence of the quarter waveplate just before the retroreflecting mirror in Fig. 5 serves to orthogonally polarize the double-shifted order with respect to the incident beam, enabling the separation of the double-passed and incident beams at a polarizing beamsplitter (PBS 2 for the

pump, PBS 3 for the probe).

### C. Frequency tuning pump and probe to EIT window

The frequency-tuning of the laser for implementing Zeeman EIT is achieved in two steps. First, the laser is tuned to the  $5^2S_{1/2}, F_g = 2 \rightarrow 5^2P_{1/2}, F_e = 1$   $^{87}\text{Rb}$  D1 transition, using the method of saturated absorption spectroscopy (SAS). Next, the pump and probe beams are fine-tuned to the  $m_{F_g} = 2, 0$  and  $m_{F_e} = 1$  Zeeman sub-levels with the AOMs (see Fig. 4(b)).

SAS is performed in a second vapor cell, located inside the box marked SAS in Fig. 5, but not explicitly shown. This cell is at room temperature, is filled with natural abundance Rb vapor (72%  $^{85}\text{Rb}$ , 28%  $^{87}\text{Rb}$ ), has no buffer gas, and the walls are uncoated. The panel in Fig. 6 shows the transmission spectrum of a weak beam diverted from the ECDL into the SAS cell, where the D1 transitions for the two Rb isotopes are displayed in one continuous scan. In plot (a), the Doppler-broadened D1 transitions are shown, before SAS is performed. Only for the  $^{87}\text{Rb}$  D1  $F_e$  states does the level separation of 815 MHz exceed the Doppler broadening  $\Gamma_D/2\pi$  for Rb vapor (see Sec. 3C), enabling the two excited states to be resolved. The  $^{85}\text{Rb}$  D1 transitions, with their smaller  $F_e$  separations, are totally smeared out by Doppler broadening. However, when SAS is performed, by introducing in the cell a strong beam that is spatially overlapped with the weak beam but counter-propagating, the absorption is saturated for the velocity-class of atoms that travels in a direction perpendicular to both the strong and weak beams. The hyperfine transitions are revealed as narrow “holes” that are “burnt” into the Doppler-broadened absorption spectra - these holes are manifested as “bumps” in the transmission spectrum in Fig. 6(b). In plot (c) the Doppler component is subtracted away and the vertical scale is magnified. The laser is tuned to the  $F_g = 2 \rightarrow F_e = 1$   $^{87}\text{Rb}$  D1 peak in plot (c) by reducing the scan to zero, while staying centered on this particular feature, and the goal of SAS is achieved. Note that some atoms that have a velocity component, say, along one of the laser beams, may be down-shifted into resonance with that beam on a particular D1 transition, while being simultaneously up-shifted into resonance with the counter-propagating beam on the higher adjacent D1 transition - this results in “crossover” peaks midway between adjacent D1 transitions. See Ref. [38] for further details on SAS.

In order to obtain EIT transmission spectra such as those shown in Fig. 8, the frequencies of the pump and probe beams in Fig. 5 need to be further fine-tuned into resonance with the Zeeman sub-levels  $m_{F_g} = 0 \rightarrow m_{F_e} = 1$  and  $m_{F_g} = 2 \rightarrow m_{F_e} = 1$ , respectively (see Fig. 4(b)). This fine-tuning is achieved inside the magnetically shielded vapor cell in Fig. 5. This is the Rb-Ne vapor cell in which the slow light experiments are carried out, the one described in Sec. 3B and C. The magnetic field  $B_z$  for Zeeman splitting is created by the solenoid in Fig. 5. Details on the Rb-Ne vapor cell are provided in Sec. 5, and on the magnetic shielding and solenoid in Sec. S2 of the Supplementary Materials. We must take into account the fact that the Zeeman shifts between the magnetic sub-levels of the  $F_g = 2$  ground state are 0.7 kHz/mG. [25] In our experiments,  $B_z = 50$  mG, yielding a Zeeman splitting between adjacent ground sub-states of 35 kHz. Because the SAS procedure described above tunes the ECDL frequency before the laser was split into pump and probe, this means that if the pump happens to be in resonance with the  $m_{F_g} = 0 \rightarrow m_{F_e} = 1$  transition, the probe (which is at the same frequency) is detuned from the  $m_{F_g} = 2 \rightarrow m_{F_e} = 1$  probe transition by  $\Delta_p = 70$  kHz (position A in Fig. 7). Scanning the probe AOM frequency ( $A \leftrightarrow C$ ) symmetrically about position B in Fig. 7, where the probe detuning  $\Delta_p = 0$  (or more precisely, where the two-photon detuning is zero; see Sec. 2D), yields EIT resonance spectra as displayed in Fig. 8. For the slow light experiments, the scan is reduced to zero while staying centered at B.

It is worth noting that, before the strong (co-propagating) pump is turned on, the weak probe experiences an absorption profile in the Rb-Ne vapor cell that resembles Fig. 6(a). In Sec. 3C we estimated the linewidth  $\gamma_{13}$ , arising from Doppler and collisional broadening in the Rb-Ne cell, for the D1 transitions to be comparable

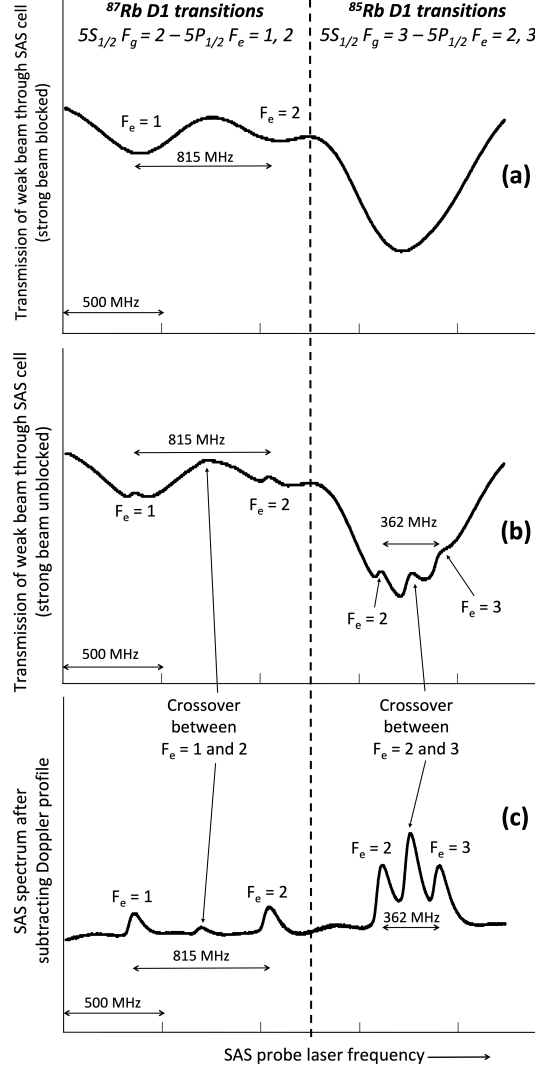


Fig. 6. Tuning the ECDL to the  $5^2S_{1/2}, F_g = 2 \rightarrow 5^2P_{1/2}, F_e = 1$   $^{87}\text{Rb}$  D1 transition via saturated absorption spectroscopy. (a) Transmission spectrum for a weak beam propagating through a Rb vapor cell with uncoated walls and no buffer gas (placed inside the box marked SAS in Fig. 5). The Doppler broadened D1 transitions in  $^{85}\text{Rb}$  and  $^{87}\text{Rb}$  are displayed in one continuous scan. The  $F_e = 2$  and 3 transitions in  $^{85}\text{Rb}$  are obscured, but the  $F_e = 1$  and 2 transitions in  $^{87}\text{Rb}$  are resolved owing to their large separation of 815 MHz. (b) A strong counter-propagating beam is introduced, revealing the hyperfine structure, even more clearly in (c) by subtracting away the Doppler component and magnifying the vertical scale. [38]

to those shown in Fig. 6(a) (see Fig. 2(a)). Turning on the strong co-propagating pump activates the narrow EIT window predicted by Fig. 2(b), and observed in Fig. 8. It is clear from Fig. 6(a) that even though the  $F_g = 2 \rightarrow F_e = 1$   $^{87}\text{Rb}$  D1 transition is advantageous for slow light experiments because this particular transition has the least spectral overlap with neighboring D1 transitions, some residual overlap of the  $F_e = 1, 2$  levels is visible. This suggests it is likely there is leakage of atoms from the  $F_e = 1$  to the  $F_e = 2$  level in the Rb-Ne vapor cell, resulting in a diminished dark state population and a reduced EIT contrast.

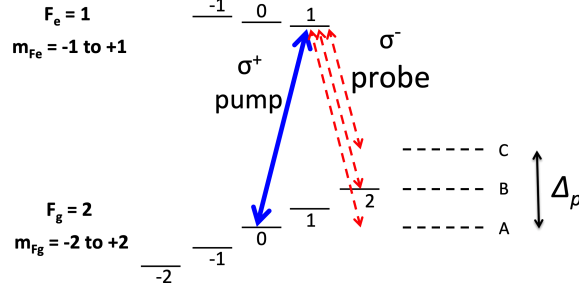


Fig. 7. Fine-tuning the pump and probe laser frequencies to the  $m_{F_g} = 0 \rightarrow m_{F_e} = 1$  and  $m_{F_g} = 2 \rightarrow m_{F_e} = 1$  sub-levels, respectively. Tuning the ECDL via SAS may put the pump in resonance with the pump transition but leave the probe, which is at the same frequency, detuned from the probe transition by  $\Delta_p = 70$  kHz (position A). EIT resonance is achieved by fine-tuning the probe frequency with the probe AOM so that  $\Delta_p$  is reduced to zero (position B). Scanning the probe frequency symmetrically about B generates the EIT spectra such as shown in Fig. 8.

#### D. Pump and probe beam size and pump intensity

The probe beam is Gaussian with a  $1/e^2$ -radius of 1.13 mm (the distance from the center of the beam where the intensity drops to  $1/e^2$  of its value at the center). To approximate an ideal plane wave (see Sec. 1 in Supplementary Notes) the pump beam, which is also Gaussian, is expanded to a  $1/e^2$ -radius of 2.26 mm using a telescope comprising two simple plano-convex lenses mounted in a cage assembly (see Fig. 5). The pump intensity was mostly varied between 1.25 and 5.6 mW/cm<sup>2</sup>, though in a few cases it was as low as 0.15 mW/cm<sup>2</sup> (compare to  $I_{sat}$ , see Sec. 3C).

#### E. Probe and reference pulses and probe intensity

In our experiments, the probe beam is in the form of a short (temporal) Gaussian pulse. Slow light demonstrations consist of measurements of the delay of the probe pulse propagating through the sample relative to an identical reference pulse propagating along a similar path-length outside the sample. This reference pulse, depicted by the dotted lines in Fig. 5, is split off from the probe pulse by inserting a non polarizing beamsplitter NPBS 4 into the probe path, as shown. The probe and reference pulses are created by amplitude modulation of the probe AOM: The probe RF amplifier output is pulsed on and off by pulsing the input from its waveform generator. It is straight-forward to measure time-delays between the centers of temporal Gaussian pulses.

Matching the reference pulse path-length to the probe path is a loose requirement because it takes light only about a nanosecond to travel 30 cm in air - this is negligible compared to the delay induced by the slowing down of the light in our experiment (tens of microseconds, see Sec. 7). The reference and probe pulses are eventually made incident on the same photodetector, and the delay in their arrival times is measured on an oscilloscope by blocking one pulse while the other is detected.

From Sec. 2F, the durations of the Gaussian probe and reference pulses must be long enough that the pulse frequency-bandwidth (estimated as the inverse of the  $1/e$ -pulse-duration  $\tau_p$ ) fits inside the EIT spectral window  $\Gamma_{EIT}$ . According to Eq. (9) the EIT linewidth broadens linearly with pump intensity, necessitating probe pulses of progressively longer duration as the pump intensity decreases. For convenience, we keep the probe pulse duration constant, and select a suitably long duration, for which the frequency bandwidth fits inside the EIT line width for the full range of pump intensities (see Sec. 6 and 7D for details).

The probe intensity must be kept significantly less than the pump, in order to satisfy the weak probe

assumption. However, the probe pulse is too short to register on a typical power-meter. Therefore, we illuminated a fast photodiode with continuous-wave light of known intensity, and calibrated the response in volts (as measured on an oscilloscope) per mW. Next, the probe pulse was shone upon the diode and the shape of the voltage response recorded. In our case the pulses have a  $1/e$ -width of  $170\ \mu\text{s}$ , and the peak of the probe Gaussian temporal waveform is set at  $0.3\ \text{mW}/\text{cm}^2$  (the average intensity of the probe pulse is  $0.12\ \text{mW}/\text{cm}^2$ ).

#### *F. Leakage of pump beam into the detected probe mode*

The pump and probe beams are recombined at polarizing beamsplitter PBS 5, so that the pump is reflected while the probe is transmitted toward the Rb-Ne vapor cell. A half-wave plate, placed in each beam before PBS 5, adjusts the relative intensity of the pump and probe beams. Because of the large pump beam size, its half-wave plate (10 mm diameter) is located before the beam expander. PBS 5 has the property that 99.5% of  $s$ -polarization (light polarization normal to plane of incidence) is reflected whereas only 90% of  $p$ -polarized light (light polarization parallel to plane of incidence) is transmitted. In our setup,  $s$  is vertical polarization (perpendicular to the optics table surface) and  $p$  is horizontal (parallel to the table surface). For this reason the pump beam, which must be strong, is chosen to be  $s$ -polarized, and the probe is  $p$ -polarized.

The combined beams, which are orthogonal-linearly-polarized, are passed through a quarter-wave plate (QP 1 in Fig. 5) and converted to orthogonal-circularly-polarized before entering the vapor cell, as is required for the Zeeman EIT  $\Lambda$ -scheme. Irises are inserted to assist in day-to-day alignments. A second quarter-wave plate (QP 2) placed after the vapor cell converts the  $\sigma^+$  and  $\sigma^-$  polarizations back to linear polarization so that the pump can be separated from the probe at a polarizing beamsplitter (PBS 6). A half-wave plate placed just after QP 2 is adjusted so that the probe transmits through PBS 6 and is focused onto a photodiode, while the pump is reflected away. The probe transmission spectrum is recorded via a fast photodiode connected to a digital oscilloscope. The impedance of the detector is kept low ( $10\ \text{k}\Omega$ ) in order to reduce electrical reflections in the BNC cable between the detector and oscilloscope, at the cost of reduced overall voltage signal.

It is obviously important to suppress as much as possible leakage of the strong pump beam into the detector at polarizing beamsplitter PBS 6. Polarizing beamsplitter cubes typically provide an extinction of  $10^3:1$ . For the highest pump powers used in our experiment, we find that a 0.1% pump leakage at PBS 6 more than doubles the power in the detected probe mode. Further, pump leakage may distort the shape of the probe pulse because the pump-profile is not entirely flat. A cleaner probe signal is obtained by the use of a Glan-Thompson polarizer (extinction ratio  $10^5:1$ ) as PBS 6 for pump-probe separation. Despite careful attempts to minimize the pump light from leaking into the probe detector, we observed some residual pump leakage. We suspect this is due to the use of low-order wave plates (as opposed to more expensive zero-order wave plates) and to residual errors in the alignment of QP1 and QP2's optical axes.

## **5. Magnetically shielded warm vapor cell**

For our slow light experiments we use a pyrex glass vapor cell, that is a sealed cylinder of 25 mm diameter, containing a small amount of isotopically pure solid  $^{87}\text{Rb}$  metal, along with 10 Torr of Ne buffer gas. Heating the cell is a convenient way to controllably vary the Rb atomic concentration in the vapor phase, yielding a few  $\mu\text{Torr}$  of  $^{87}\text{Rb}$  vapor. A heater assembly is used to vary the cell temperature from  $55^\circ\text{C}$  to  $65^\circ\text{C}$  during the experiment, thus varying the Rb atomic number density  $N$  participating in EIT between  $1.5 \times 10^{11}\ \text{cm}^{-3}$  and  $3.4 \times 10^{11}\ \text{cm}^{-3}$  (see Supplementary Materials, Sec. S2). The length of the cell (28 mm) includes 1.6 mm windows (not anti-reflection coated) on either end. Therefore the length of the vapor sample  $L$  is taken to be 25 mm. The cell is placed inside a solenoid as shown in Fig. 5. To enable Zeeman EIT, the solenoid



applies a small magnetic field  $B_z = 50$  mG, co-linear with the laser beam propagation. The cell, solenoid, and heater assembly are placed inside a magnetic shield in order to suppress stray magnetic fields incident on the sample below 0.2 mG, i.e.,  $< 0.5\%$  of  $B_z$  (see Supplementary Materials, Sec. S2).

## 6. Setting the probe pulse bandwidth

In order to observe slow light we need to ensure that the probe (and reference) pulse bandwidth is less than the EIT spectral window  $\Gamma_{EIT}$ . The EIT spectrum is obtained by the procedure described in Sec. 4C.

Typical EIT linewidths measured for high and low pump intensities, as a function of the probe detuning  $\Delta_p$ , are shown in Fig. 8. The maximum contrast measured (for the high intensity) is only  $\sim 25\%$ , for reasons

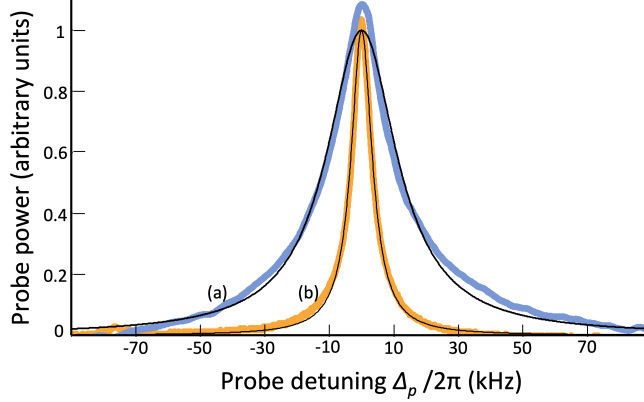


Fig. 8. (a) Measured EIT lineshapes (thick lines) in a few  $\mu$ Torr of isotopically pure  $^{87}\text{Rb}$  vapor with 10 Torr Ne at  $65^\circ\text{C}$ , for pump intensity a)  $I = 5.5$  mW/cm $^2$  ( $\Omega_c/2\pi = 3.9$  MHz), and b)  $I = 1.3$  mW/cm $^2$  ( $\Omega_c/2\pi = 1.9$  MHz). The FWHM, extracted by Lorentzian fits (thin lines), are 26 kHz and 7.3 kHz, respectively.

explained in Sec. 2D and Sec. 3B. In order to enable a visual linewidth comparison between the lineshapes obtained at high and low intensities, we normalized the lineshapes and displayed them on the same vertical scale. By fitting with a Lorentzian, we observe EIT linewidths of 7.3 kHz and 26 kHz for  $I = 1.3$  mW/cm $^2$  and 5.5 mW/cm $^2$ , respectively, which correspond to  $\Omega_c/2\pi$ -values of 1.9 MHz and 3.9 MHz, respectively (see Sec. 3C). Data are spectrally narrower at the center of the Lorentzian owing to coherent contributions from atoms that diffuse in and out of the laser beam multiple times without decohering (this is known as Ramsey-narrowing). [5, 33]

We chose a  $1/e$ -width of 170  $\mu$ s for our Gaussian probe and reference pulses (see Sec. 4E). The corresponding bandwidth of  $\leq 1$  kHz fits inside the EIT window which, from Eq. (9), is at least  $2\gamma_{12}/2\pi \approx 6$  kHz wide even for the smallest pump intensities.

Generating a EIT lineshape measurement as in Fig. 8 typically takes 40 ms for the higher pump intensities, and 160 ms for the lower intensities (we set the AOM for a  $\pm 100$  kHz frequency-sweep in 10 ms; each spectrum in Fig. 8 is an average of either 4 or 16 such sweeps). Our laser system's passive stabilization yields a frequency drift of  $< 10$  MHz/hour, resulting in a drift of less than 0.5 kHz while generating these EIT data-profiles.

## 7. Results and discussion

In order to create short pulses, the probe frequency scan is now turned off, the probe AOM offset voltage is tuned to the EIT peak, and the amplitude modulation is turned on, as described in Sec. 4E. Once both slow and reference pulses are detected on an oscilloscope, the temporal waveform for each is fit to a gaussian curve, and the relative delay time  $\tau_d$  is extracted. Typical measurements of  $\tau_d$  are presented in Fig. 9, where

the data (fuzzy lines) are shown along with Gaussian fits (smooth lines).

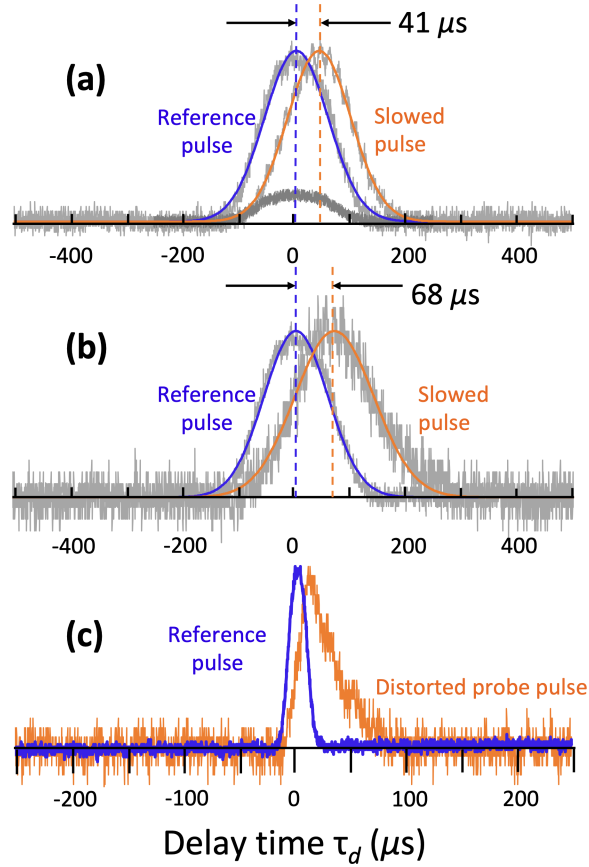


Fig. 9. Measurement of time-delay  $\tau_d$  between reference and probe pulses traveling through air and the EIT medium, respectively. a)  $\tau_d = 41 \mu\text{s}$  yields  $v_g = 610 \text{ m/s}$ . Pump intensity  $I = 3 \text{ mW/cm}^2$ . The squat data-curve is the transmitted probe pulse when the pump is blocked, in which case EIT ceases so that large absorption occurs with no slowing. b)  $\tau_d = 68 \mu\text{s}$  yields  $v_g = 368 \text{ m/s}$ , our slowest observed velocity. Pump intensity  $I = 1.2 \text{ mW/cm}^2$ . c) Significant distortion in the transmitted probe pulse occurs if we select a pulse duration so narrow that the probe bandwidth does not fit inside the EIT transparency window. All measurements are in  $^{87}\text{Rb}$  vapor with 10 Torr Ne at  $65^\circ\text{C}$ .

In Figs. 9(a) and (b) the reference pulse arrives at the detector earlier than the probe by  $\tau_d = 41 \mu\text{s}$  and  $68 \mu\text{s}$ , respectively, which corresponds to a slowed probe group velocity  $v_g$  of 610 m/s and 368 m/s (using  $v_g = L/\tau_d$ ). In each case, the peaks of the fits for reference and probe are scaled to the same value for easier comparison. The reference and probe pulse intensities are similar at the non-polarizing beamsplitter NPBS4 in Fig. 5, but the probe pulse suffers some absorption in the vapor (recall that our EIT contrast never exceeds 25%) which explains the increased noise on the slowed pulses. The slower group velocity was achieved by lowering the pump intensity which further reduces the overall signal-to-noise ratio.

#### A. Observed $\Gamma_{\text{EIT}}$ , $\tau_d$ , and $v_g$ vs. theoretical prediction

To predict the EIT linewidth  $\Gamma_{\text{EIT}}$  we insert in Eq. (9) parameter-values that are relevant to our experiment, as discussed in Sec. 3C:  $\gamma_{12}/2\pi \approx 3 \text{ kHz}$ ,  $\gamma_{13}/2\pi \approx 300 \text{ MHz}$ . The optical depth is estimated using  $N = 3.4 \times 10^{11} \text{ cm}^{-3}$  and  $L = 2.5 \text{ cm}$  (see Sec. 5), yielding  $OD \approx 25$ . For control intensities  $I$  of 1.3 and 5.5

mW/cm<sup>2</sup>, corresponding to  $\Omega_c/2\pi = 1.9$  and 3.9 MHz (see Sec. 6), we find that Eq. (9) predicts  $\Gamma_{EIT}/2\pi = 10.8$  and 26.3 kHz, respectively, remarkably close to the observed values in Fig. 8.

To predict the delay time  $\tau_d$  and the slowed probe group velocity  $v_g$ , we refer to Eq. (13) and Eq. (14), which use just the power-broadened component of  $\Gamma_{EIT}$ . For intensities  $I = 3$  mW/cm<sup>2</sup> and 1.2 mW/cm<sup>2</sup> as in Fig. 9, the calculated delays  $\tau_d$  are 72  $\mu$ s (yielding a predicted  $v_g$  of 347 m/s) and 181  $\mu$ s (predicted  $v_g = 138$  m/s), respectively. The predicted  $v_g$ -values are a factor two to three slower than the observed  $v_g$ -values in Fig. 9 (a) and (b). To make more accurate predictions, we must move away from an idealized three-level atom model and include the full hyperfine structure (Fig. 3), which is beyond the scope of this article. [18]

### B. Role of EIT transparency window

Fig. 9(a) highlights the importance of the EIT process. The squat data-waveform is the transmitted probe pulse when the pump beam is blocked causing the EIT window to cease to exist: Large absorption and no slowing is observed. The transmitted power of the slow pulse for the unblocked pump is  $\sim 20 - 25\%$  of the incident probe power, while for the blocked pump is less than 5%.

To further highlight the important role played by EIT, we show in Fig. 9(c) what happens if we select a pulse duration for which the probe bandwidth does not fit inside the EIT transparency window. The input Gaussian pulse in this case, namely  $\sim 20\mu$ s (which yields a  $1/e$ -pulse bandwidth of  $\sim 10$  kHz), is nearly an order of magnitude shorter than the 170  $\mu$ s pulse employed in Fig. 9(a) and (b). Thus, in the case of Fig. 9(c) the pulse bandwidth is comparable to the EIT window which ranges from a few kHz to  $\leq 30$  kHz for our experiments. The frequency components of this pulse that do not fit within the EIT window are not slowed, and are instead significantly absorbed. This leads to a significant temporal stretching and distortion of the pulse, as shown in Fig. 9(c) (we scaled the vertical size of the reference pulse to about the same as the transmitted probe).

In fact, some probe pulse broadening is visible even in the case of the slowest group velocity measured in Fig. 9(b). In this case, higher frequency components of the 170  $\mu$ s Gaussian probe pulse ( $1/e$ -frequency bandwidth  $\sim 1$  kHz) extrude past the 7.3 kHz Lorentzian EIT transparency window, and are strongly absorbed. This causes an effective narrowing of the probe bandwidth, which leads to a broadening of the pulse duration.

### C. Slow group velocity vs. pump intensity

In Fig. 10 we plot the experimentally observed slow light group velocity for several pump intensities at three different vapor temperatures. The observed temperature-dependence of  $v_g$  is in accordance with what we

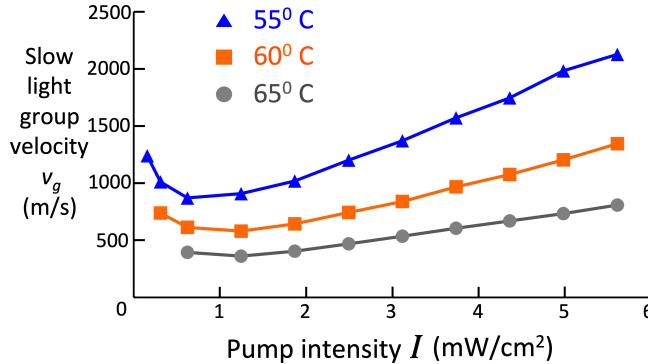


Fig. 10. Slow light at different pump intensities  $I$  and temperatures  $T$  (lines drawn to guide the eye). All measurements are in isotopically pure <sup>87</sup>Rb vapor with 10 Torr Ne.

expect from Eq. (13):  $N$  increases with  $T$  (see Sec. S2 D in supplementary materials), causing  $v_g$  to decrease.

At a fixed temperature we surmise from Fig. 10 that two competing slow light effects occur when we vary the pump intensity. The linear increase of  $v_g$  with increasing pump intensity  $I$  is expected from Eq. (13). Recall that this originates from the power-broadening of the EIT transparency window as described by Eq. (9), thereby reducing the “tightness of the pinch” of the “wrinkle” in the real refractive index  $n_r$  at  $\Delta_p = 0$  in Figs. 2 (d,f). However, it is obvious that one cannot keep reducing the pump intensity to achieve lower and lower group velocities as there is no slow light in the absence of a pump.

At really low pump intensities, the weak probe assumption starts to break down and, as mentioned in Sec. 3C already, the population of atoms being pumped to the dark state may decline to the point that the probe pulse appears to start speeding up again.

Group velocities of several thousand m/s suffice for most cutting-edge experiments on quantum memory and image storage in warm vapor. [5, 6] At higher temperatures, the density increases, but so do spin depolarization mechanisms such as Rb-Rb spin exchange collisions and radiation trapping, as indicated in Sec. 3B. In vapor cells that use paraffin-based anti-spin relaxation coatings instead of buffer gas, temperatures exceeding 80°C may cause coating breakdown. Coatings such as OTS (octadecyltrichlorosilane) permit higher temperatures. [39, 40]

## 8. Conclusion

We have presented detailed theoretical and experimental undergraduate-friendly instructions on how to produce light pulses propagating through warm alkali vapor with speeds as low as few hundred m/s. We elucidated the role played by EIT in producing slow light.

The experimental setup described here is remarkably versatile. It can be used for investigations into slow and stored light, including detailed measurements of pulse delay  $\tau_d$  as the pulse width  $\tau_p$  is varied, and further measurement of the subtle Ramsey narrowing seen at the EIT line-center in Fig. 8 as the pump and probe beam sizes are varied. [33] By slightly varying the angle between the pump and probe beams, one can study EIT linewidth-narrowing due to the spatial localization of alkali atoms from frequent velocity-changing collisions with the buffer gas. [41] Furthermore, one may study how atomic diffusion degrades storage times for slow light pulses [42] of various transverse profiles, e.g., Laguerre-Gaussian [43] and Bessel beams [44], which possess topological phase features that permit significantly more robust storage in comparison to the usual Gaussian beams. The setup may be adapted for innovative magnetometry with potential applications in magnetic induction tomography and the detection of concealed objects. [45, 46]

## 9. Acknowledgements

We acknowledge support by the U. S. Army Research Office under grant number W911NF2110120. We appreciate insightful discussions with Drs. Irina Novikova, David Phillips, Ofer Firstenberg, and Ran Finkelstein, and detailed invaluable feedback from three anonymous referees. We thank Hong Cai, Kaleb Campbell, Richard Jackson, Dillon deMedeiros, Bradley Worth, Amanda Day, Somaya Madkhaly, Yuhong (Iris) Zhang, Peter Harnish, and Jason Barkeloo for help during the initial setup. We thank the Miami University Instrumentation Laboratory for crucial help in machining and electronics. The authors have no conflicts to disclose.

<sup>†</sup> These two authors contributed equally.

\* Corresponding author: balis@miamioh.edu

## References

1. L. V. Hau, S. E. Harris, Z. Dutton, and C. H. Behroozi, “Light speed reduction to 17 metres per second in an ultracold atomic gas,” *Nature* **397**, 594 - 596 (1999)
2. M. Kash, V. Sautenkov, A. Zibrov, L. Hollberg, G. Welch, M. Lukin, Y. Rostovtsev, E. Fry, and M. Scully, “Ultralow group velocity and enhanced nonlinear optical effects in a coherently driven hot atomic gas,” *Phys. Rev. Lett.* **82**, 5229 - 5232 (1999)
3. S. Harris, J. Field, and A. Imamoglu, “Nonlinear optical processes using electromagnetically induced transparency,” *Phys. Rev. Lett.* **64**, 1107 - 1110 (1990)
4. S. Harris, “Electromagnetically induced transparency,” *Physics Today* **50**, 36 (1997)
5. I. Novikova, R. Walsworth, Y. Xiao, “Electromagnetically induced transparency-based slow and stored light in warm atoms,” *Laser Photonics Rev.* **6**, 333 - 353 (2012)
6. L. Ma, O. Slattery, and X. Tang, “Optical quantum memory based on electromagnetically induced transparency,” *J. Opt.* **19**, 043001, 1-24 (2017)
7. M. Afzelius, N. Gisin, and H. de Riedmatten, “Quantum memory for photons,” *Phys. Today* **68** (12) 42 - 47 (2015)
8. C. Adams, J. Pritchard, J. Schaffer, “Rydberg atom quantum technologies,” *J. Phys. B* **53**, 012002(1-13)(2020)
9. N. Belcher, E. Mikhailov, I. Novikova, “Atomic clocks and coherent population trapping: Experiments for undergraduate labs,” *Am. J. Phys.* **77**, 988 - 998 (2009)
10. See, for example, A. Zheng, A. Green, M. Crescimanno, and S. O’Leary, “Electromagnetically-induced-transparency intensity-correlation power broadening in a buffer gas,” *Phys. Rev. A* **93**, 043825 (1-6) (2016)
11. A. J. Olson and S. K. Mayer, “Electromagnetically induced transparency in rubidium,” *Am. J. Phys.* **77** (2), 116 - 121 (2009)
12. T. Pang, “Electromagnetically induced transparency,” *Am. J. Phys.* **69** (5), 604 - 606 (2001)
13. K. McDonald, “Slow light,” *Am. J. Phys.* **68**(3), 293 (2000)
14. “Slow, Stored, and Stationary Light,” M. Fleischhauer, G. Juzeliūnas, 359-385, “Optics in our time,” Springer (2016); eds: M. Al-Amri, M. El-Gomati, M. Zubairy
15. P. W. Milonni and J. H. Eberly, *Laser Physics* (Wiley, Hoboken, 2010); See Sec. 9.10, pp 441 - 446
16. B. E. A. Saleh and M. Teich, *Fundamentals of Photonics* (Wiley, 1991)
17. Our definition of  $\Omega_c, \Omega_p$  follows Refs. [5,15,18]. Some authors omit the 2 in the denominator (e.g., [25,27]).
18. M. Lukin, M. Fleischhauer, A. Zibrov, H. Robinson, V. Velichansky, L. Hollberg, and M. Scully, “Spectroscopy in dense coherent media: Line narrowing and interference effects,” *Phys. Rev. Lett.* **79**, 2959 - 2962 (1997)
19. M. Fleischhauer and M. Lukin, “Quantum memory for photons: Dark-state polaritons,” *Phys. Rev. A* **65**, 022314 (1-12) (2002)
20. Eq. (14) is identical to Eq. (6) in Ref. [5], Eq. (38) in [19].
21. M. Klein, M. Hohensee, Y. Xiao, R. Kalra, D. Phillips, and R. Walsworth, “Slow-light dynamics from electromagnetically induced transparency spectra,” *Phys. Rev. A* **79**, 053833 (1-3) (2009)
22. Eq. (15) is identical to Eq. (39) in Ref. [19].
23. N. B. Phillips, A. V. Gorshkov, and I. Novikova, “Optimal light storage in atomic vapor,” *Phys. Rev. A* **78**, 023801 (1-10) (2008)
24. M. Hosseini, B. M. Sparkes, P. K. Lam, and B. C. Buchler, “High efficiency coherent optical memory with warm rubidium vapor,” *Nature Commun.* **2**, 174 (1-5) (2011)

25. <https://steck.us/alkalidata/>, D. Steck, University of Oregon
26. See Fig. 7.5 on pg. 141 of Ref. [27]
27. M. Auzinsh, D. Budker, and S. M. Rochester, *Optically Polarized Atoms* (Oxford University Press, New York, 2010)
28. W. Happer, “Optical pumping,” *Rev. Mod. Phys.* **44** (2), 169 - 249 (1972)
29. J. E. Thomas and W. W. Quivers, Jr., “Transit-time effects in optically pumped coupled three-level systems,” *Phys. Rev. A* **22** (5), 2115 - 2121 (1980)
30. E. Arimondo, “Relaxation processes in coherent population trapping,” *Phys. Rev. A* **54** (3), 2216 - 2223 (1996)
31. A. Matsko, I. Novikova, M. Scully, and G. Welch, “Radiation trapping in coherent media,” *Phys. Rev. Lett.* **87** (13), 133601 (1-4) (2001)
32. See Ref. [15], Sec. 4.11 or Ref. [27], Sec. 9.1
33. Y. Xiao, I. Novikova, D. F. Phillips, and R. Walsworth, “Diffusion-induced Ramsey narrowing,” *Phys. Rev. Lett.* **96**, 043601 (1-4) (2006)
34. M. Shuker, O. Firstenberg, Y. Sagi, A. Ben-kish, N. Davidson, and A. Ron, “Ramsey-like measurement of the decoherence rate between Zeeman sublevels,” *Phys. Rev. A* **78**, 063818 (1-7) (2008)
35. M. D. Rotondaro and G. P. Perram, “Collisional broadening and shift of the rubidium D1 and D2 lines ( $5^2S_{1/2} \rightarrow 5^2P_{1/2}, 5^2P_{3/2}$ ) by rare gases,  $H_2$ ,  $D_2$ ,  $N_2$ ,  $CH_4$  and  $CF_4$ ,” *Journal of Quantitative Spectroscopy and Radiative Transfer* **57**, 497 - 507 (1997)
36. See, for example, Ref. [15], Sec. 3.9, pp 105 - 108
37. See Fig. 5 and accompanying text in J. Kleykamp, A. Hachtel, D. Kane, M. Marshall, N. Souther, P. Harnish, and S. Bali, “Measurement of sub-natural line width AC Stark shifts in cold atoms: An experiment for an advanced undergraduate laboratory,” *Am. J. Phys.* **79**(12), 1211 - 1217 (2011)
38. A. Hachtel, J. Kleykamp, D. Kane, M. Marshall, B. Worth, J. Barkeloo, J. Kangara, J. Camenisch, M. Gillette, and S. Bali, “An undergraduate measurement of radiative broadening in atomic vapor,” *Am. J. Phys.* **80** (8), 740 - 743 (2012); *ibid.* **81**(6), 471 (2013)
39. R. Finkelstein, private communication; see also “Technical Info” on the Precision Glassblowing, Inc. website
40. H. Chi, W. Quan, J. Zhang, L. Zhao, and J. Fang, “Advances in anti-relaxation coatings of alkali-metal vapor cells,” *Appl. Surf. Sci.* **501**, 143897 (1-15) (2020)
41. M. Shuker, O. Firstenberg, R. Pugatch, A. Ben-Kish, A. Ron, and N. Davidson, “Angular dependence of Dicke-narrowed electromagnetically induced transparency resonances,” *Phys. Rev. A* **76**, 023813 (1-5) (2007)
42. M. Shuker, O. Firstenberg, R. Pugatch, A. Ron, and N. Davidson, “Storing images in warm atomic vapor,” *Phys. Rev. Lett.* **100**, 223601 (1-4) (2008)
43. R. Pugatch, M. Shuker, O. Firstenberg, A. Ron, and N. Davidson, “Topological stability of stored optical vortices,” *Phys. Rev. Lett.* **98**, 203601 (1-4) (2007)
44. S. Smartsev, R. Chriki, D. Eger, O. Firstenberg, and N. Davidson, “Structured beams invariant to coherent diffusion,” *Opt. Express* **28** (22), 33708 - 33717 (2020)
45. A. Wickenbrock, F. Tricot, F. Renzoni, “Magnetic induction measurements using an all-optical  $^{87}\text{Rb}$  atomic magnetometer,” *Appl. Phys. Lett.* **103**, 243503 (1-4) (2013)
46. C. Deans, L. Marmugi, and F. Renzoni, “Through-barrier electromagnetic imaging with an atomic magnetometer,” *Opt. Express* **25** (15), 17911 - 17917 (2017)